Monthly Notices
of the
ROYAL ASTRONOMICAL SOCIETY

MNRAS **430,** 2249–2261 (2013) doi:10.1093/mnras/stt045

Feeding versus feedback in AGNs from near-infrared IFU observations: the case of Mrk 79

Rogemar A. Riffel,[1]⋆ Thaisa Storchi-Bergmann[2] and Claudia Winge[3]

[1]*Universidade Federal de Santa Maria, Departamento de Física, Centro de Ciências Naturais e Exatas, 97105-900, Santa Maria, RS, Brazil*
[2]*Universidade Federal do Rio Grande do Sul, Instituto de Física, CP 15051, Porto Alegre 91501-970, RS, Brazil*
[3]*Gemini Observatory, c/o Aura, Inc., Casilla 603, La Serena, Chile*

Accepted 2013 January 7. Received 2013 January 7; in original form 2012 November 19

ABSTRACT

We have mapped the gaseous kinematics and the emission-line flux distributions and ratios from the inner ≈680 pc radius of the Seyfert 1 galaxy Mrk 79, using two-dimensional (2D) near-infrared *J*- and K_1-band spectra obtained with the Gemini instrument Near-Infrared Integral Field Spectrograph at a spatial resolution of ≈100 pc and velocity resolution of ≈40 km s^{-1}. The molecular hydrogen H_2 flux distribution presents two spiral arms extending by ≈700 pc, one to the north and another to the south of the nucleus, with an excitation indicating heating by X-rays from the central source. The low-velocity dispersion ($\sigma \approx 50$ km s^{-1}) and rotation pattern supports a location of the H_2 gas in the disc of the galaxy. Blueshifts observed along the spiral arm in the far side of the galaxy and redshifts in the spiral arm in the near side, suggest that the spiral arms are feeding channels of H_2 to the inner 200 pc. From channel maps along the H_2 λ2.1218 μm emission-line profile we estimate a mass inflow rate of $\dot{M}_{H_2} \approx 4 \times 10^{-3}$ M$_\odot$ yr^{-1}, which is one order of magnitude smaller than the mass accretion rate necessary to power the active galactic nucleus (AGN) of Mrk 79. The emission from the ionized gas (traced by Paβ and [Fe II] λ1.2570 μm emission lines) is correlated with the radio jet and with the narrow-band [O III] flux distribution. Its kinematics shows both rotation and outflows to the north and south of the nucleus. The ionized gas mass outflow rate through a cross-section with radius ≈320 pc located at a distance of ≈455 pc from the nucleus is $\dot{M}_{out} \approx 3.5$ M$_\odot$ yr^{-1}, which is much larger than the AGN mass accretion rate, indicating that most of the outflowing gas originates in the interstellar medium surrounding the galaxy nucleus, which is pushed away by a nuclear jet.

Key words: galaxies: individual: Mrk 79 – galaxies: ISM – galaxies: kinematics and dynamics – galaxies: Seyfert – infrared: galaxies.

1 INTRODUCTION

This work is part of a large project, in which our group (Active Galactic Nuclei Integral Field Spectroscopy – AGNIFS) has been observing the inner kiloparsec of nearby active galaxies using optical and near-infrared (hereafter near-IR) high-spatial resolution (a few to tens of pc) integral field spectroscopy. We have obtained the gaseous flux distributions, kinematics and excitation, with the main goal of mapping gas inflows and outflows and constraining the corresponding mass flow rates and power. Whenever the signal-to-noise (S/N) ratio in the continuum and absorption lines is high enough we also map the stellar kinematics and ages. In the near-IR, our main results so far can be summarized as follows. We have found that the molecular (H_2) and ionized gases present distinct flux distributions and kinematics, with the former restricted to the plane of the galaxy and presenting, in some cases, streaming motions towards the nucleus, while the latter presents emission from outflowing material at high latitudes above the plane and usually is associated with the radio emission (Riffel et al. 2006a, 2008, 2009; Storchi-Bergmann et al. 2009, 2010; Riffel, Storchi-Bergmann & Nagar 2010; Riffel & Storchi-Bergmann 2011a). We have concluded that the molecular gas is a good tracer of the nuclear feeding and the ionized gas of its feedback. Nevertheless, the sample observed so far comprises only half a dozen objects and more integral field observations in the near-IR are required in order to have a more complete census of these processes in active galactic nuclei (AGNs) and to relate the mass flow rates to the AGN power.

In this work, we present the gaseous flux distribution and kinematics of the inner 680 pc of the active galaxy Mrk 79 obtained from

⋆ E-mail: rogemar@ufsm.br

observations using the Gemini-North's Near-Infrared Integral Field Spectrograph (NIFS; McGregor et al. 2003) in the *J* and *K* bands. This object was selected for this study because it presents extended radio and [O III] emission (e.g. Ulvestad & Wilson 1984; Nagar et al. 1999; Schmitt et al. 2003) allowing us to explore the relation between the radio jet and the narrow-line region (NLR) kinematics, as well as its effect in the excitation of the near-IR lines.

Mrk 79 is a SBb galaxy (de Vaucouleurs et al. 1991) located at a distance of 93.8 Mpc (e.g. Kraemer et al. 2011), for which 1 arcsec corresponds to 455 pc at the galaxy. Its nucleus is classified as Seyfert 1 with a central black hole with a mass of $5.2 \pm 1.44 \times 10^7\,M_\odot$ (Peterson et al. 2004). It presents extended radio-continuum emission along a position angle (PA) of 11° (Ulvestad & Wilson 1984; Nagar et al. 1999; Schmitt et al. 2001), which can be described as an asymmetric triple radio structure with the northern source being located at a distance of 800 pc from the nucleus and the southern source at 460 pc from it (Schmitt et al. 2001). In the optical, Mrk 79 presents extended [O III] line emission as observed in ground-based (e.g. Haniff, Wilson & Ward 1988) and *Hubble Space Telescope* (*HST*) images (Schmitt et al. 2003). The [O III] λ5007 emission extends to about 4.6 arcsec from the nucleus in the north–south direction, being cospatial with the radio emission and presenting several blobs of enhanced emission (Schmitt et al. 2003). An outflowing gas component is suggested by the detection of two components in the [O III] λ5007 emission-line profile with velocities of +100 and −50 km s^{-1} relative to the systemic velocity of the galaxy. This component seems to be associated with the northern radio structure (Whittle et al. 1988). The modelling of the optical and infrared spectral energy distribution of Mrk 79, including the emission by dust in a toroidal-like structure heated by a central AGN suggests that the dusty torus has a mass of $7.30 \times 10^2\,M_\odot$ (Fritz, Franceschini & Hatziminaoglou 2006).

This paper is organized as follows. In Section 2, we describe the observations and data reduction procedures. The results are presented in Section 3 and discussed in Section 4. We present our conclusions in Section 5.

2 OBSERVATIONS AND DATA REDUCTION

The *J* and K_l-band observations of Mrk 79 were obtained using the NIFS instrument (McGregor et al. 2003) operating with the Gemini North Adaptive Optics system altitude conjugate adaptive optics for the infrared (ALTAIR) in 2010 September under the programme GN-2010B-Q-42, following the standard object-sky–sky-object dither sequence, with off-source sky positions since the target is extended, and individual exposure times of 520 s for the *J* band and 550 s for the K_l band. Six on-source individual exposures were obtained for each band, totalizing 3120 and 3300 s for the *J* and K_l-band, respectively.

The *J*-band observations covered the spectral region from 1.14 to 1.36 μm, centred at 1.25 μm with a spectral resolution of ≈1.8 Å, as obtained from the measurement of the full width at half-maximum (FWHM) of the ArXe calibration lamp lines. The K_l-band observations were centred at 2.3 μm, covering the spectral range from 2.10 to 2.53 μm with a spectral resolution of FWHM ≈ 3.5 Å. In velocity space, the resolution of the observations is ≈45 km s^{-1} for the K_l band and 35 km s^{-1} for the *J* band.

The data reduction was accomplished using tasks contained in the NIFS package which is part of GEMINI IRAF package, as well as generic IRAF tasks. The reduction procedure included trimming of the images, flat-fielding, sky subtraction, wavelength and s-distortion calibrations. We have also removed the telluric bands and flux calibrated the frames by interpolating a blackbody function to the spectrum of the telluric standard star. The six individual data cubes of each band were median combined to a single data cube using the *gemcombine* task of the GEMINI IRAF package, with a *sigclip* algorithm to eliminate the remaining cosmic rays and bad pixels. The final Integral Field Unit (IFU) data cube in each band contains ∼4000 spectra, each spectrum corresponding to an angular coverage of 0.05 arcsec × 0.05 arcsec, which translates into ∼23 × 23 pc^2 at the galaxy and covering the inner 3 arcsec × 3 arcsec (∼1.35 × 1.35 kpc^2).

In order to increase the S/N ratio and allow the fitting of the emission-line profiles, we have replaced each spatial pixel by the median of its value and that of its first eight neighbours. After this procedure, the angular resolution, obtained from the FWHM of the spatial profile of the broad components of Brγ and Paβ emission lines fluxes, is 0.25 arcsec ± 0.05 arcsec for both bands, corresponding to ∼100 pc at the galaxy.

3 RESULTS

In order to illustrate the spatial coverage of our observations, we show in the top-left panel of Fig. 1 a *V*-band optical image of Mrk 79 obtained with the 1 m telescope of the Lick Observatory (Hunt et al. 1999). In the top-right panel we present an [O III] λ5007 Å narrow-band image obtained with the *HST* Wide Field Planetary Camera 2 (WFPC2) through the filter FR533N (Schmitt et al. 2003). This image shows extended emission up to 4 arcsec from the nucleus of Mrk 79, being more elongated along a PA of 15° and presenting several blobs of emission. Schmitt et al. (2003) suggest that the [O III] emission is related to the radio jet. The 3.6 cm radio continuum image obtained with the Very Large Array (VLA) by Schmitt et al. (2001) is shown in the bottom-left panel of this figure, and can be described as an asymmetric triple radio structure along PA = 11°. The green box overplotted on this panel represents the NIFS field of view and shows that the north-eastern radio structure is beyond its borders. The Paβ flux map obtained from our NIFS data cube is shown in the bottom-right panel in units of 10^{-17} erg s^{-1} cm^{-2}.

All spectra in the data cube were first corrected for redshift. In Fig. 2 we present the *J* and K_l spectra extracted within a 0.25 arcsec × 0.25 arcsec aperture centred on the nucleus in the top panels. The middle panels show the spectra extracted at 1.1 arcsec south-southeast of the nucleus at the location where it is observed as a knot with enhanced emission in the [O III] image in the top-right panel of Fig. 1, while the bottom panels show the spectra for a location cospatial with the southern radio hotspot seen in bottom-left panel of Fig. 1 at 11. arcsec south-southwest of the nucleus. Some of the strongest emission lines are identified in the top panels.

We have detected about 4 dozen of emission lines at the *J* and K_l bands as listed in Table 1, which presents the corresponding fluxes of the lines for the three positions above. The observed emission lines include molecular (H_2) lines as well as lines of ionized gas from a range of ionization levels, e.g. from [Fe II] up to [S IX]. The line fluxes were measured by fitting a Gaussian to each emission-line profile using the IRAF SPLOT task. The uncertainties quoted in the table are the standard deviations from the average of several measurements (typically 6) and do not include uncertainties in the flux calibration of the spectra. Flux values followed by '?' indicate that the line is only marginally detected, with a large uncertainty, of the order of the line flux. The presence of the line is supported by the fact that it has the expected central wavelength and the fact that the width is similar to that of the other emission lines.

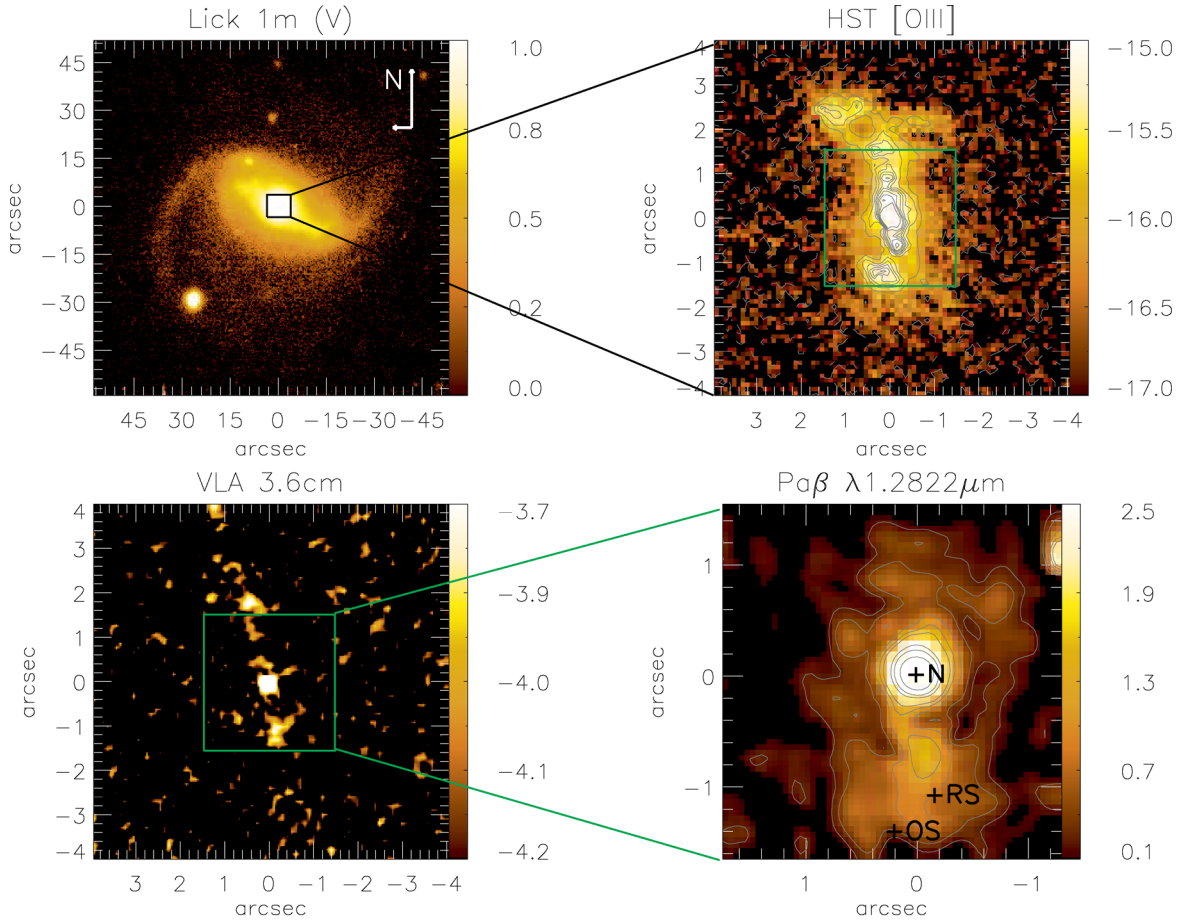

Figure 1. Top-left: *V*-band optical image of Mrk 79 obtained with the 1 m telescope of the Lick Observatory (Hunt et al. 1999). Top-right: [O III] λ5007 Å image obtained with the *HST* (Schmitt et al. 2003). Bottom-left: 3.6 cm radio continuum image obtained with the VLA by Schmitt et al. (2001). The green box overlaid to this panel represents the NIFS field of view. Bottom-right: Paβ flux map obtained from our NIFS data cube in units of 10^{-17} erg s^{-1} cm^{-2}. The positions labelled as N, RS and OS mark the location of the nucleus, the southern radio spot and the southern [O III] southern blob, respectively.

3.1 Emission-line flux distributions

In order to construct maps for the flux distribution of the strongest emission lines, we used the PROFIT routine (Riffel 2010) to integrate the fluxes under the profiles of [P II] λ1.1886 μm, [S IX] λ1.2526 μm, [Fe II] λ1.2570 μm, Paβ, H_2 λ2.1218 μm and Brγ emission lines and subtract the underlying continuum. These particular lines have been chosen because they have the highest S/N ratios among their species (coronal lines, forbidden and permitted ionized gas lines and molecular lines). We were unable to construct maps for the flux distributions of He I, He II and [Ca VIII] emission lines because they are detected only at a few locations of the observed field. The broad components for Paβ and Brγ were fitted and subtracted before the construction of the flux maps in these emission lines.

Fig. 3 shows the resulting flux maps for each emission line (identified at the top of each panel). The central cross marks the position of the nucleus defined as the peak of the near-IR continuum emission, the cyan contours overlaid to the [Fe II] map are from the radio continuum image from Schmitt et al. (2001), shown in the top-right panel of Fig. 1. The green contours overlaid to the Paβ flux map are from the [O III] image of Schmitt et al. (2003), shown in the bottom-left panel of Fig. 1. The lower flux level shown in each panel corresponds to 3σ, where σ is the noise in the adjacent continuum to the line.

The coronal line [S IX] λ1.2526 μm (top-middle panel of Fig. 3) emission is marginally resolved by our observations (with FWHM ≈ 0.35 arcsec) being more extended along the north–south direction with flux peak at the nucleus. A similar behaviour is observed for the [P II] flux distribution (top-left panel), with an additional emission from a region located at 1.1 arcsec south of the nucleus, almost cospatial with the southern radio hotspot seen in Fig. 1. The [Fe II] emission is extended up to 1.4 arcsec from the nucleus, showing two structures at the highest flux levels: one at the nucleus and another cospatial with the southern radio hotspot. Lower level emission is observed surrounding these structures.

The Paβ and Brγ flux maps show extended emission up to the borders of the NIFS field to the north and to the south, while in the east–west direction it extends only to ≈0.5 arcsec from the nucleus. The H I emission seems to be well correlated with the [O III] structures, as evidenced by the contours of the [O III] image overlaid on the Paβ flux map. Finally, the H_2 also presents extended emission more elongated in the north–south direction, but with a distinct flux distribution than those observed for the other emission lines. The H_2 map clearly shows two spiral arms extending up to 1.5 arcsec from the nucleus, which seem to originate from the tips of a nuclear bar-shaped structure oriented approximately along east–west, observed at the highest flux levels.

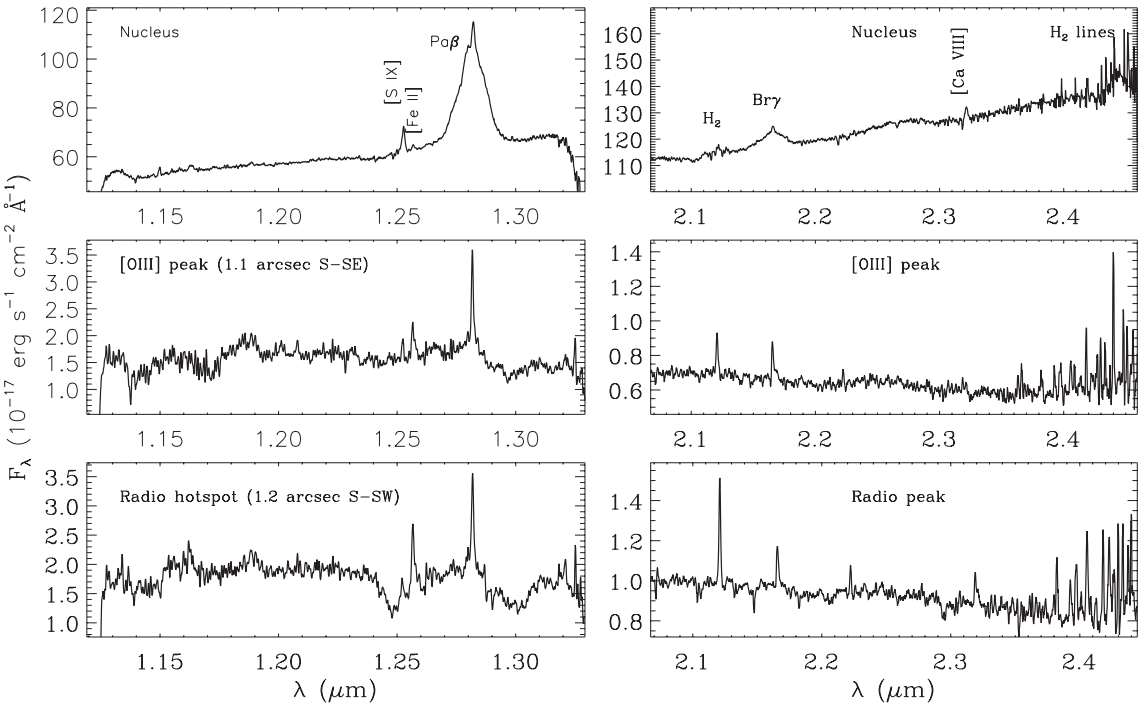

Figure 2. Sample of spectra for Mrk 79 extracted within square apertures of 0.25 arcsec × 0.25 arcsec, with the stronger emission lines identified. Top panels show the nuclear *J* (left) and *K* (right) spectrum, middle panels show a spectrum for a location at 1.2 arcsec south-southeast of the nucleus, cospatial with an [O III] emission knot and the bottom panels present a spectrum extracted at the position of the radio structure at 1.2 arcsec south-southwest of the nucleus. These positions are identified in Fig. 1 as 'N', 'OS' and 'RS', respectively.

Table 1. *J*-band emission-line fluxes for the nucleus, the position of an [O III] blob (at 1.1 arcsec south-southeast of the nucleus) and the position of the radio hotspot (at 1.2 arcsec south-southwest of the nucleus) integrated within 0.25 arcsec × 0.25 arcsec apertures. The location where each spectrum was extracted is identified in the bottom-left panel of Fig. 1 as N (for the nucleus), OS ([O III] structure) and RS (radio structure). The fluxes are in 10^{-17} erg s^{-1} cm^{-2} units. A '?' by the side of the flux value indicates that the line is detected but the uncertainty in the measurement is of the order of the flux of the line.

λ_{vac}(μm)	ID	Nucleus	[O III] peak	Radio peak
1.12708	[Fe II] $b^2F_{5/2} - b^4F_{5/2}$	–	–	2.45 ± 1.18
1.13488	[Fe II] $b^2D_{3/2} - a^2F_{7/2}$	–	1.54?	3.17 ± 0.84
1.14276	[Fe II] $b^4D_{5/2} - b^4F_{9/2}$	–	–	0.61?
1.14713	[P II] $^1D_3 - ^3P_1$	32.39 ± 1.97	–	1.87?
1.15841	[Fe II] $b^2F_{5/2} - a^2D_{3/2}$	7.13?	1.95?	
1.16296	He II 7−5	43.71 ± 7.75	–	5.23 ± 1.51
1.18363	[Fe II] $b^4D_{5/2} - b^4F_{5/2}$	5.29?	0.76?	–
1.18552	He II 29−7	–	1.28?	–
1.18693	[Fe II] $b^4D_{3/2} - b^4F_{5/2}$	–	1.44?	–
1.18861	[P II] $^1D_2 - ^3P_2$	17.30 ± 5.85	3.00 ± 0.28	4.57 ± 0.77
1.20370	He II 26−7	–	0.77?	1.18?
1.20545	[Fe II] $a^4D_{3/2} - a^6F_{7/2}$	5.73?	–	–
1.22263	[Fe II] $a^4D_{1/2} - a^6D_{5/2}$	8.78?	2.02?	1.19?
1.24414	[Fe II] $c^2G_{9/2} - a^4G_{11/2}$	–	–	0.97?
1.25235	[S IX] $^3P_1 - ^3P_2$	161.97 ± 7.91	3.99 ± 0.25	2.55 ± 0.71
1.25702	[Fe II] $a^4D_{7/2} - a^6D_{9/2}$	26.79 ± 7.33	8.12 ± 1.99	13.20 ± 0.29
1.27069	[Fe II] $a^4D_{1/2} - a^6D_{1/2}$	–	1.32?	–
1.27912	[Fe II] $a^4D_{3/2} - a^6D_{3/2}$/He I?	–	1.39?	0.71?
1.28216	H I Paβ (broad)	5666.25 ± 164.06	–	–
1.28216	H I Paβ (narrow)	154.28 ± 15.41	16.34 ± 0.61	16.56 ± 1.04
1.28495	He I $^3S_1 - ^3Po_1$	–	1.40?	0.87?
1.29812	[Fe II] $a^4D_{3/2} - a^6D_{1/2}$	11.85 ± 3.30	–	0.39?
1.30529	[Fe II] $c^2G_{9/2} - a^4G_{9/2}$	–	1.46?	0.59?
1.31958	[Fe II] $b^2G_{7/2} - b^4F_{9/2}$	–	–	1.36?
1.32092	[Fe II] $a^4D_{7/2} - a^6D_{7/2}$	–	2.46?	3.50?

Table 1 – *continued*

λ_{vac}(μm)	ID	Nucleus	[O III] peak	Radio peak
2.12183	H_2 1-0 S(1)	89.89 ± 23.19	4.42 ± 0.09	8.85 ± 0.74
2.15420	H_2 1-0 S(2)	–	–	0.80?
2.16612	H I Brγ(broad)	1054.40 ± 159.49	–	–
2.16612	H I Brγ (narrow)	48.96 ± 9.36	4.08 ± 0.72	3.21 ± 0.27
2.17661	[Fe II] $b^2G_{7/2} - b^2H_{11/2}$	22.06?	–	–
2.18911	He II 10−7	–	1.53 ± 0.08	–
2.22344	H_2 1-0 S(0)	19.51 ± 6.74	1.35 ± 0.13	2.14 ± 0.35
2.24776	H_2 2-1 S(1)		–	1.39 ± 0.34
2.26647	[Fe II] $b^2G_{7/2} - b^2H_{9/2}$	–	0.59?	–
2.32204	[Ca VIII] $^2P^0_{3/2} - ^2P^0_{1/2}$	165.60 ± 38.37	–	3.50 ± 0.65
2.36760	[Fe II] $a^4G_{9/2} - a^4H_{9/2}$	–	2.43?	–
2.39901	[Fe II] $b^4D_{7/2} - a^2F_{7/2}$	–	3.90 ± 0.21	4.79?
2.40847	H_2 1-0 Q(1)	–	2.75 ± 0.22	6.81 ± 0.50
2.41367	H_2 1-0 Q(2)	–	1.01?	–
2.42180	H_2 1-0 Q(3)	–	4.28 ± 0.06	5.20 ± 0.21
2.43697	H_2 1-0 Q(4)	–	2.61?	–
2.46075	He II 18−9	–	8.20 ± 1.41	–

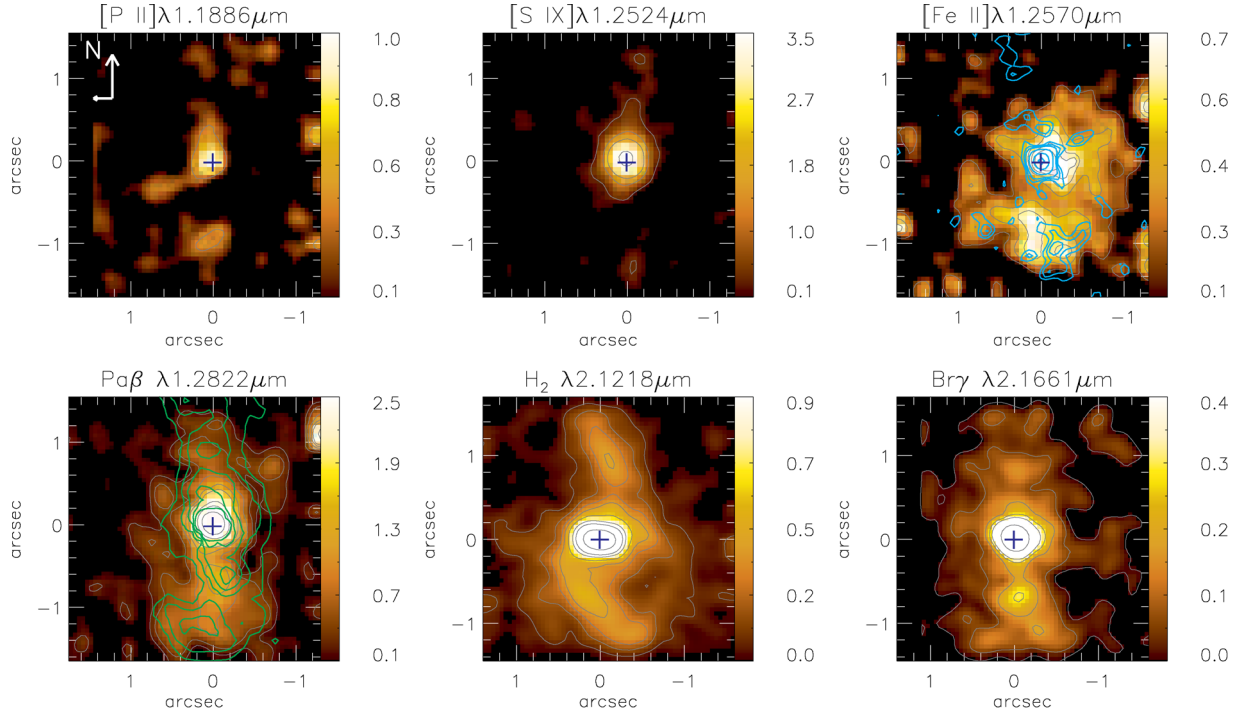

Figure 3. Emission-line flux distributions for [P II] λ1.1886 μm, [S IX] λ1.2526 μm, [Fe II] λ1.2570 μm, Paβ, H_2 λ2.1218μm and Brγ emission lines. The colour bars show the flux scale in units of 10^{-17}erg s^{-1}cm^{-2}. The central cross marks the position of the nucleus, the cyan contours overlaid to the [Fe II] map are from the 3.6 cm radio-continuum image of Schmitt et al. (2001) and the green contours overlaid to the Paβ map are from the [O III] image of Schmitt et al. (2003).

3.2 Line-ratio maps

Line ratios can be used to study the extinction and the excitation mechanisms of the near-IR lines in the NLR (e.g. Rodríguez-Ardila, Riffel & Pastoriza 2005; Riffel, Rodríguez-Ardila & Pastoriza 2006b; Rodríguez-Ardila et al. 2006; Storchi-Bergmann et al. 2009; Riffel et al. 2010; Riffel & Storchi-Bergmann 2011b; Dors et al. 2012).

The reddening can be estimated from the Paβ/Brγ line ratio as

$$E(B-V) = 4.74 \log\left(\frac{5.88}{F_{Pa\beta}/F_{Br\gamma}}\right), \quad (1)$$

where $F_{Pa\beta}$ and $F_{Br\gamma}$ are the fluxes of *Pa*β and *Br*γ emission lines, respectively. We have used the reddening law of Cardelli, Clayton & Mathis (1989) and adopted the intrinsic ratio $F_{Pa\beta}/F_{Br\gamma} = 5.88$ corresponding to case B recombination (Osterbrock & Ferland 2006). The resulting $E(B-V)$ map is shown in the left-hand panel of Fig. 4. This map shows a very complex structure with several knots of higher extinction, in which $E(B-V)$ reaches values of up to 2.

The excitation mechanism of the [Fe II] lines can be investigated using the [Fe II]λ1.2570 μm/Paβ line ratio, shown in the middle panel of Fig. 4. Typical values for this ratio are [Fe II]λ1.2570 μm/Pa$\beta \approx 0.6$, observed over most of the field. The

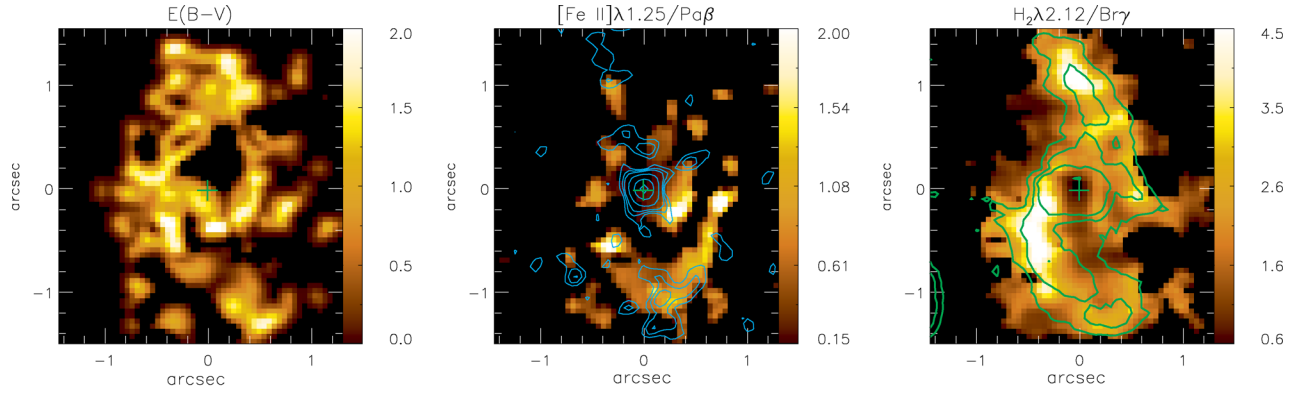

Figure 4. Emission-line ratio maps. Left: $E(B-V)$ obtained from Paβ/Brγ line ratio. Middle: [Fe II]λ1.2570 μm/Paβ. Right: H$_2\lambda$2.1218 μm/Brγ. The contours overlaid to the [Fe II]λ1.2570 μm/Paβ are for the radio image and to the H$_2\lambda$2.1218 μm/Brγ for the H$_2$ flux map of Fig. 3.

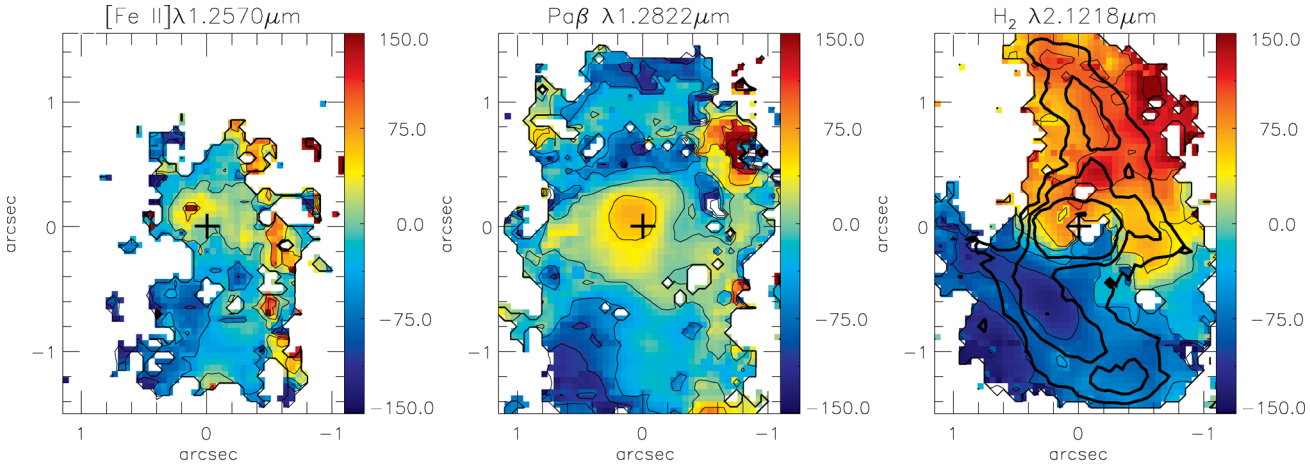

Figure 5. Centroid velocity fields for the [Fe II]λ1.2570 μm (left), Paβ (middle) and H$_2$ λ2.1218 μm (left) emitting gas. The central crosses mark the position of the nucleus, north is up and east left and the thick contours overlaid to the H$_2$ map are from the H$_2$ flux image of Fig. 3. Only the inner 1.2 arcsec in the east–west direction is shown.

lowest values are observed at the nucleus (≈0.15), while the highest values of up to 2 are observed to the southwest at ≈0.4 arcsec from the nucleus and in an arc-shaped structure at ≈1 arcsec. At the location of the southern ratio hotspot (cyan contours are from the radio image) the average value for this ratio is 1.2.

A useful line ratio to study the excitation mechanism of the near-IR H$_2$ lines is H$_2\lambda$2.1218 μm/Brγ. We present a map for this ratio in the right-hand panel of Fig. 4. The highest values of up to 4.5 are observed along the two spiral arms seen in the H$_2$ flux map shown in the bottom-middle panel of Fig. 3, overlaid as green contours in the line-ratio map. The lowest values, around 0.6, are observed at the nucleus and at locations away from the spiral structures.

3.3 Centroid velocity and velocity dispersion maps

The PROFIT routine (Riffel 2010) was used to fit the emission-line profiles by Gaussian curves in order to obtain the centroid velocity (V) and velocity dispersion (σ), which have been used to map the gas kinematics in the inner region of Mrk 79. We used the [Fe II]λ1.2570 μm, Paβ and the H$_2\lambda$2.1218 μm emission lines to represent the kinematics of the ionized and molecular gas. We do not show kinematic maps for the [P II], [S IX] and Brγ lines (as done for flux maps) because these lines are detected only in a few regions and the Brγ kinematics is the same as that of Paβ.

In Fig. 5, we present the velocity fields obtained from the centroid wavelength of [Fe II]λ1.2570 μm (left-hand panel), Paβ (middle) and H$_2\lambda$2.1218 μm (right). The uncertainties in velocity are smaller than 15 km s^{-1} for all emission lines at all locations of the field. The white regions in this figure represent locations where the S/N was not high enough to allow the fitting of the line profiles. We subtracted the heliocentric systemic velocity ($V_s \approx 6636$ km s^{-1}), obtained from the fitting of the H$_2$ velocity field by a rotating disc model (e.g. Riffel & Storchi-Bergmann 2011a,b). The thick contours overlaid to the H$_2$ velocity map are from the H$_2\lambda$2.12 flux image, shown in Fig. 3. These maps show that the [Fe II] and Paβ emitting gas present similar velocity fields, with redshifts of about 40 km s^{-1} at the nucleus and blueshifts of up to −150 km s^{-1} both to the north and to the south. The Paβ map also shows some redshifts in a region located at ≈1.0 arcsec northwest of the nucleus, with velocities of 150 km s^{-1}, similar to the values seen in the H$_2$ velocity field at the same location. The H$_2$ velocity field shows an approximate rotation pattern, with the highest blueshifts, of up to −150 km s^{-1}, to the southeast of the nucleus, and the highest redshifts, of up to 150 km s^{-1}, to the northwest. The contours overlaid as thick lines are from the H$_2$ flux distribution, showing that deviations from the rotation pattern are associated with the spiral arms. In particular, a region of higher blueshifts than the surrounding is seen inside the highest level contour delimiting the spiral structure to the south of the nucleus.

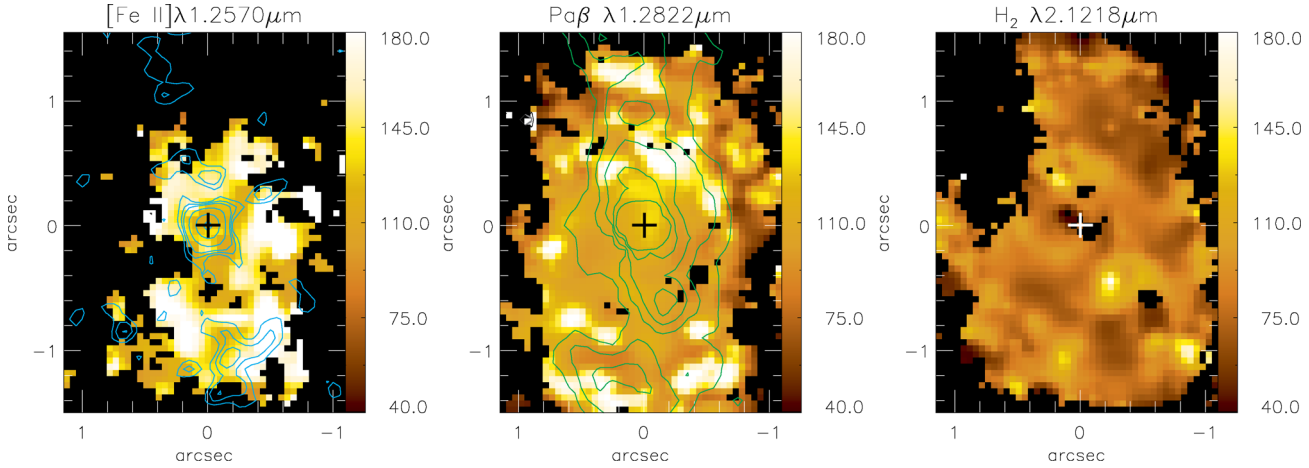

Figure 6. σ maps for the same emission lines of Fig. 5. The cyan contours overlaid to the [Fe II] map are from the 3.6 cm radio-continuum image of Schmitt et al. (2001) and the green contours overlaid to the Paβ map are from the [O III] image of Schmitt et al. (2003).

In Fig. 6, we show the velocity dispersion maps for the [Fe II]λ1.2570 μm (left-hand panel), Paβ (middle) and $H_2\lambda$2.1218 μm (right) emitting gas. Typical uncertainties in σ are of 15 km s^{-1}. For the [Fe II] and Paβ the σ values range from 40 to 180 km s^{-1}, presenting the highest values in some knots located away from the nucleus. In order to compare the [Fe II] σ and radio maps, we have overlaid the contours from the radio image on the [Fe II] σ map (cyan contours in Fig. 6). This comparison shows that the highest σ values are observed in regions surrounding the radio structures. The nuclear σ for [Fe II] and Paβ are both of the order of ≈110 km s^{-1}. The H_2 σ map is shown in the right-hand panel of Fig. 6 and presents smaller values than those observed for the Paβ and [Fe II], with typical values being 75 km s^{-1}. The smallest values (∼60 km s^{-1}) are observed in locations cospatial with the spiral structure observed in the H_2 flux map (Fig. 3), while the highest values of up to 130 km s^{-1} are observed in some knots to south and southwest of the nucleus.

3.4 Velocity channel maps

In order to map the flux distributions at all velocities covered by the emission-line profiles, including the wings, we constructed channel maps along the profiles of the [Fe II]λ1.2570 μm, Paβ and $H_2\lambda$2.1218 μm emission lines, shown in Figs 7–9, respectively. Each panel presents the flux distribution in logarithmic units integrated within the velocity bin centred at the velocity shown in the top-left corner (relative to the systemic velocity of the galaxy) and the central cross marks the position of the nucleus.

In Fig. 7, the channel maps along the [Fe II] emission-line profile show the flux distributions integrated within velocity bins of 50 km s^{-1}(corresponding to two spectral pixels). The green contours overlaid to some panels are from the radio image of Schmitt et al. (2003). The highest blueshifts of up to −200 km s^{-1} and the highest redshifts, with similar velocities, are observed at the nucleus and from a region centred at ∼1.0 arcsec to the south, where it is approximately coincident with the southern radio structure. At intermediate and zero velocities the [Fe II] emission is observed from the nucleus down to ≈1.4 arcsec to the south, still presenting the same two peaks, at the nucleus and at 1.0 arcsec to the south.

Fig. 8 shows the channel maps for the Paβ emitting gas for the same velocity bin as for [Fe II]. The green contours overlaid to some panels are from the [O III] image of Schmitt et al. (2001). At the highest blueshifts (velocities of ∼ −200 km s^{-1}) the Paβ emission arises from three structures: a 'blob' at the nucleus, one 0.7 arcsec to the south and another 1.1 arcsec to the southeast (see channel maps centred at −166 and −215 km s^{-1}) while the highest redshifts are observed at the nucleus and 0.7 arcsec to the south. At velocities between ≈ −160 and ≈ −80 km s^{-1}an additional structure is seen at 0.8 arcsec north of the nucleus. At these velocities, the Paβ emission is thus observed to both sides (north and south) of the nucleus, presenting four knots of enhanced emission, which are correlated to structures observed in the [O III] image, as can be seen from the [O III] contours overlaid to the panels at velocities ranging from −66 to 80 km s^{-1}.

The channel maps along the H_2 emission-line profile are shown in Fig. 9 for a velocity bin of 60 km s^{-1} (corresponding to two spectral pixels). At the highest blueshifts (−235 to −175 km s^{-1}), the H_2 emission originates in a spiral arm extending for about 1.0 arcsec and located southeast of the nucleus. For panels centred at velocities ranging from −175 to −54 km s^{-1}, the spiral arm curves in the direction of the nucleus, resembling the arm are seen in the H_2 flux distribution of Fig. 3. At zero velocities there is emission to both sides of the nucleus and as the velocities increase and reach positive values another spiral arm appears to the northwest. The highest redshifts of up to 400 km s^{-1} are observed at the nucleus.

4 DISCUSSION

4.1 Gaseous excitation

What is the origin of the near-IR lines of [Fe II] and H_2 from AGNs? This question has been investigated by several studies (e.g. Black & van Dishoeck 1987; Hollenbach & McKee 1989; Forbes & Ward 1993; Mouri 1994; Maloney, Hollenbach & Tielens 1996; Simpson et al. 1996; Larkin et al. 1998; Rodríguez-Ardila et al. 2004, 2005; Riffel et al. 2006a, 2010; Hicks et al. 2009; Ramos Almeida, Pérez García & Acosta-Pulido 2009; Sánchez et al. 2009; Storchi-Bergmann et al. 2009; Riffel & Storchi-Bergmann 2011b). In summary, the H_2 emission lines can be excited by two mechanisms: (i) fluorescent excitation through absorption of soft-ultraviolet photons (912–1108 Å) in the Lyman and Werner bands (Black & van Dishoeck 1987) and (ii) collisional excitation due to the heating of the gas by shocks, due to interaction of a radio jet with the interstellar medium (ISM; Hollenbach & McKee 1989) or by X-rays from

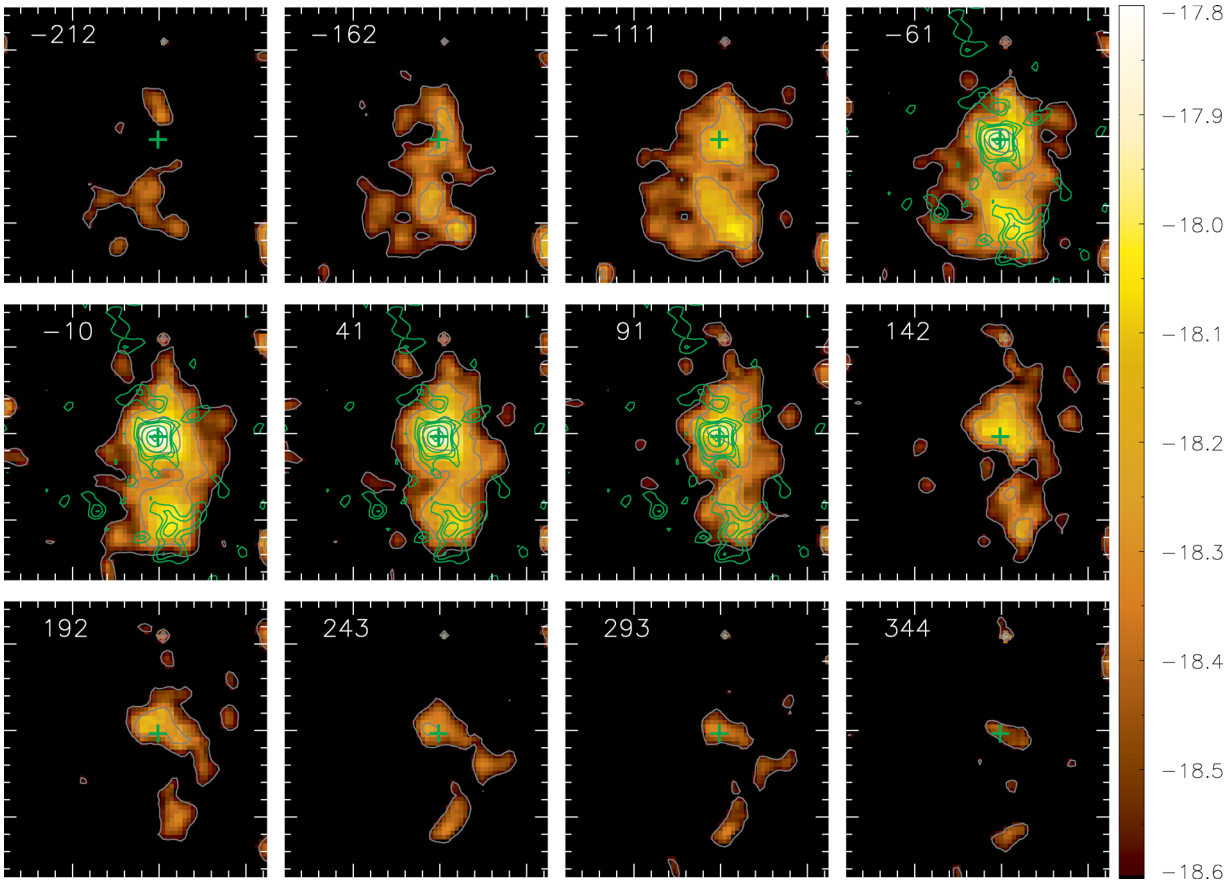

Figure 7. Channel maps along the [Fe II] emission-line profile for a velocity bin of 50 km s^{-1} and centred at the velocity shown in the top-left corner of each panel. The green contours are from the radio image of Schmitt et al. (2003) and the cross marks the position of the nucleus.

the AGN (Maloney et al. 1996). The second mechanism, usually refereed as thermal processes, is also responsible for the excitation of the near-IR lines of the [Fe II]. Most of the studies above investigate the origin of both H_2 and [Fe II] using line ratios, such as [Fe II]λ1.2570 μm/Paβ and H_2 λ2.1218 μm/Brγ, and a common conclusion among these studies is that thermal processes dominate the H_2 emission in the central region of active galaxies, while the fluorescent excitation can contribute only with a small fraction of the observed H_2 emission.

The main difficulty in the study of the excitation of the H_2 and [Fe II] in AGNs regards the distinction between X-ray and shock mechanisms. Recent detailed studies using integral field spectroscopy – most of them by our AGNIFS group – indicate that the H_2 and [Fe II] emitting gas have distinct flux distributions and kinematics, with the former being considered a tracer of the feeding of the AGN and the latter a tracer of its feedback (e.g. Riffel et al. 2006a, 2010; Hicks et al. 2009; Sánchez et al. 2009; Storchi-Bergmann et al. 2009, 2010; Riffel & Storchi-Bergmann 2011a,b). This scenario is also favoured in the case of Mrk 79. The H_2 flux distribution in the shape of two spiral arms (Fig. 3), observed also in the channel maps (Fig. 9) supports a location of the molecular gas in the plane of the galaxy. Additionally, the H_2 velocity field, shown in Fig. 5, presents a clear rotation pattern with the southeast side approaching and the northwest side receding from us. The smaller velocity dispersion values observed for H_2 (see Fig. 6), relative to those of the ionized gas, also supports that the H_2 emitting gas is more restricted to the plane of the galaxy. The [Fe II] emitting gas presents a more disturbed velocity field, higher σ values and a flux distribution well correlated with the radio structures, indicating interaction with the radio jet. The presence of both blueshifts and redshifts to the south of the nucleus at the location of the southern radio structure, suggests that the [Fe II] emitting gas extends to high galactic latitudes. The H I recombination lines present a similar velocity field to that of [Fe II], but smaller σ values (intermediate values between those of [Fe II] and H_2) and distinct flux distributions, being more associated with the [O III] emission than to the radio emission, as seen in the Figs 3 and 8. Thus, the [Fe II] kinematics supports the presence of shocks contributing to its excitation.

The emission-line ratios can also be used to investigate the gas excitation. The [Fe II]λ1.25 μm/Paβ and $H_2\lambda$2.12 μm/Brγ emission-line ratios can be used to distinguish between Seyferts, low-ionization nuclear emission-line regions (LINERs) and Starbursts (e.g. Larkin et al. 1998; Rodríguez-Ardila et al. 2004, 2005). Seyfert nuclei have values in the range $0.6 \lesssim$ [Fe II]/Paβ $\lesssim 2.0$ and $0.6 \lesssim$ H_2/Brγ $\lesssim 2.0$, while Starburst galaxies have smaller values for both ratios and LINERs have higher values (e.g. Rodríguez-Ardila et al. 2005). From the middle panel of Fig. 4, it can be seen that the [Fe II]/Paβ ratio map presents typical Seyfert values for most of the observed field. The only exception is the nucleus, where [Fe II]/Paβ ≈ 0.15, for which the Paβ flux can be increased due to contamination of the narrow component by the broad profile and thus, decreasing this ratio. The H_2/Brγ line ratio, shown in the right-hand panel of Fig. 4, presents most values in the range expected for Seyfert galaxies. Nevertheless, higher values are observed in the regions where the spiral structures are seen in the H_2 flux distribution

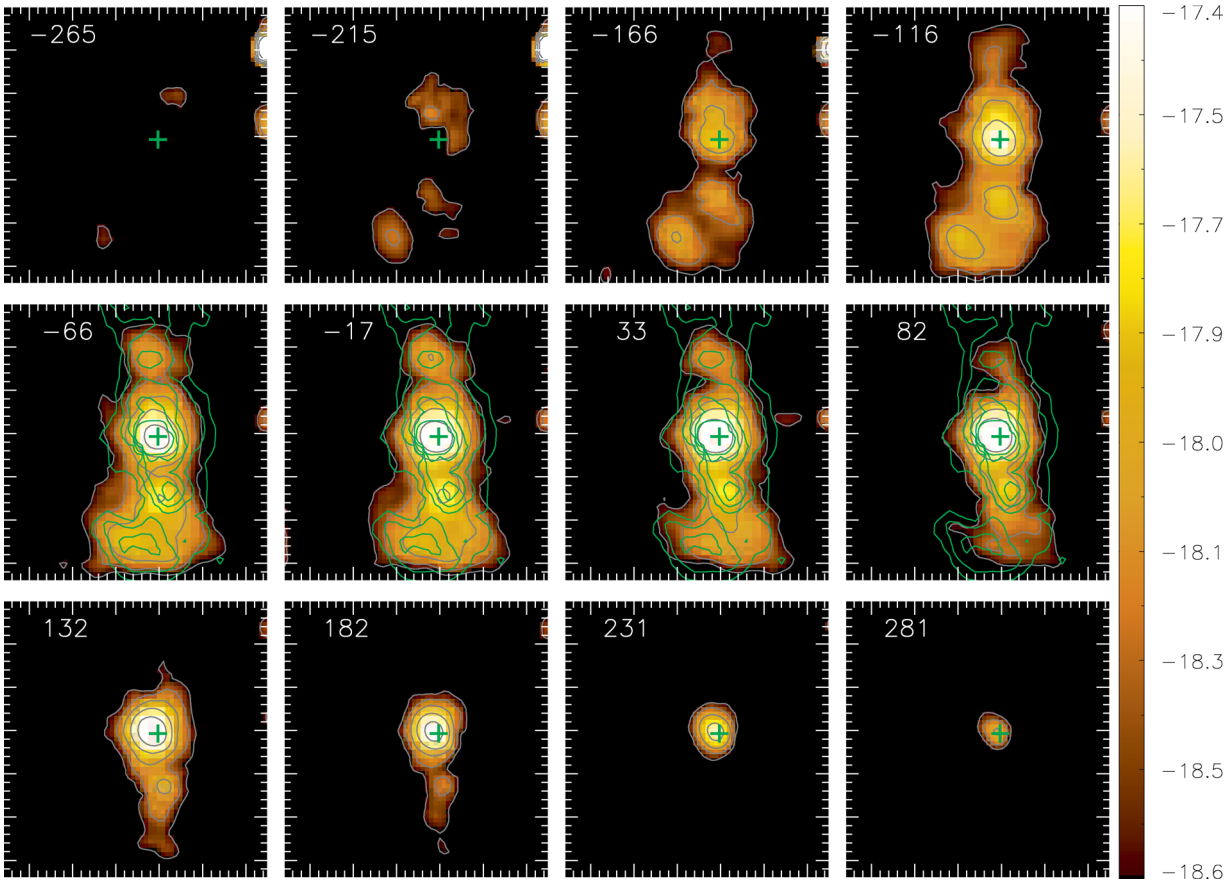

Figure 8. Same as Fig. 7 for the Paβ emission line. The green contours are from the [O III] image from Schmitt et al. (2001).

(Fig. 3) reaching $H_2/Br\gamma \approx 4.5$. These ratios can be understood by an enhancement of the H_2 emission in the spiral arms due to the increase of the gas density due to the spiral structure.

In a recent study, Dors et al. (2012) built photoionization models considering a two-component continuum, one to account for the big bump component peaking at 1 Ryd and another to represent the X-ray source that dominates the continuum emission at high energies in order to reproduce the [Fe II]λ1.25 μm/Paβ and $H_2\lambda$2.12 μm/Brγ line ratios of AGNs. The authors compared their models with the line ratios observed for a large sample of AGN from long-slit and IFU spectroscopy. They concluded that typical Seyfert values for these ratios, as those observed for Mrk 79, are well reproduced by the model and concluded that the heating by X-rays produced by active nuclei can be considered a common and very important mechanism of excitation of [Fe II] and H_2 lines. In the case of Mrk 79, such conclusion must be taken with caution since the H_2 and [Fe II] have distinct flux distribution and kinematics, suggesting that their emission originates from gas located at distinct regions of the galaxy, as discussed above. This may also be the case of the extended emission of other Seyfert galaxy (e.g. Riffel et al. 2006a, 2008, 2009, 2010; Storchi-Bergmann et al. 2009, 2010; Storchi-Bergmann 2010; Riffel & Storchi-Bergmann 2011a,b,c).

We have observed a good correlation between the [Fe II] flux distribution and the radio emission, as well as an increase of the [Fe II] σ in locations cospatial with the radio structures. This correlation is particularly clear in the channel maps shown in Fig. 7 for velocities ranging from −61 to 91 km s^{-1} – enhancements in the flux are observed at the locations of the two main radio structures: a hotspot at the nucleus and another at ≈1.2 arcsec to the south of the nucleus. This result suggests that the radio jet has an important role in the [Fe II] emission, either by releasing iron from dust grains via shocks and increasing its abundance in the gas phase or by enhancing the [Fe II] emitting gas density due to compression produced by the radio jet.

The correlation between the NLR gas emission and radio structures has been questioned in detailed studies of nearby Seyfert galaxies. Examples are the studies of the NLR kinematics of NGC 4151 (Kaiser et al. 2000; Das et al. 2005) and NGC 1068 (Das et al. 2006), using high-spatial resolution long slit spectra obtained with Space Telescope Imaging Spectrograph. The absence of any clear correlation between the optical emission lines and radio structures led the authors to conclude that there is no connection between the kinematics of the NLR and radio jets. The argument is that, even though these structures are approximately aligned as they originate in the same AGN, when the targets are close enough, high spatial resolution data show that there is no correlation between the NLR gas kinematics and the radio jet. Although we believe that this may happen in some cases, we would like to point out that in the case of NGC 4151, our study (Storchi-Bergmann et al. 2010) of the NLR kinematics using adaptive optics near-IR integral field spectroscopy, at similar spatial resolution to that of the above studies, has shown that there is interaction of the radio jet with ambient gas at low velocities. This finding was only possible because our 3D integral field spectroscopic data has a moderately high spectral resolution (∼5000), allowing us to inspect and separate the gas emission features at distinct velocities via channel maps. This separation allowed us to find this interaction of the radio jet with gas at velocities close to systemic. At the high velocity channels, an outflowing

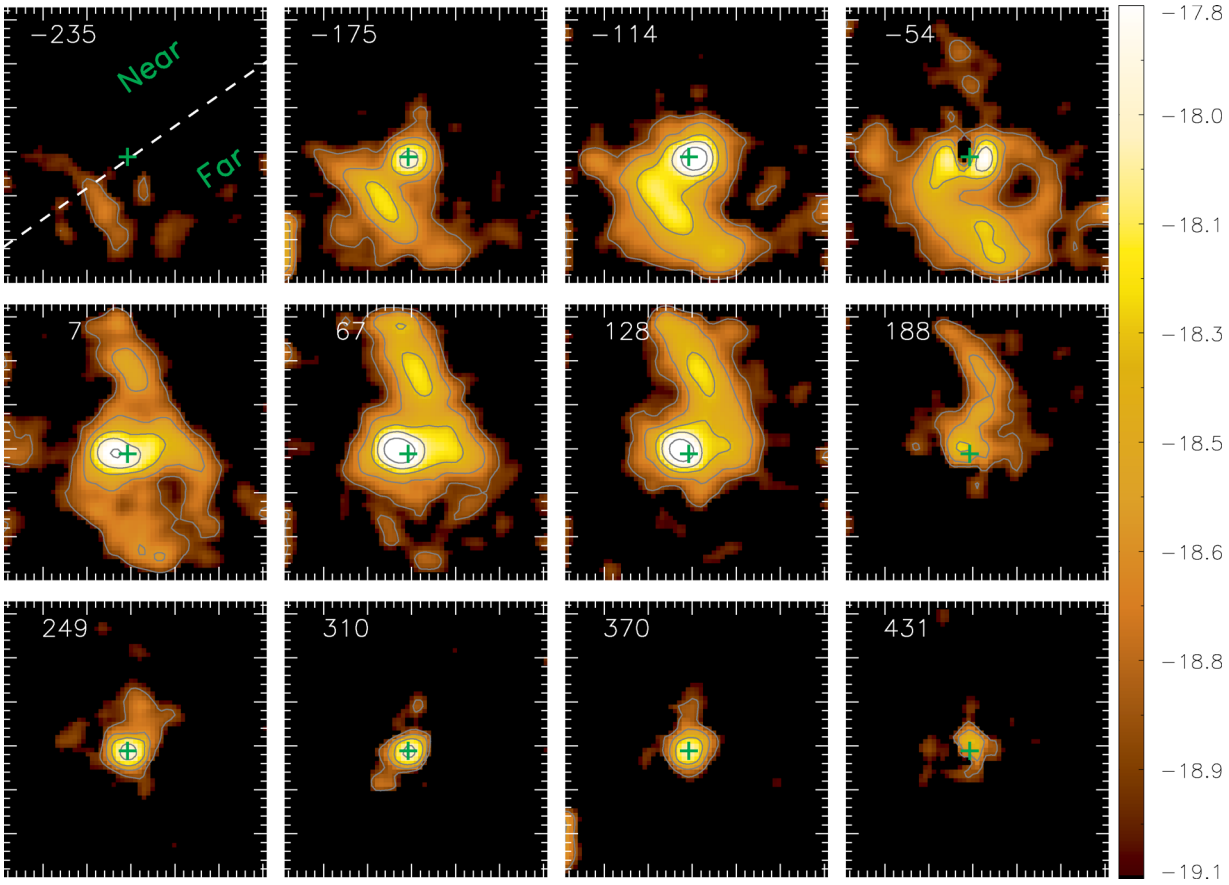

Figure 9. Same as Fig. 7 for the H_2 emission line for a velocity bin of 60 km s^{-1}.

component along the ionization cone dominates the gas emission, and does not show any correlation with the radio jet.

In the case of Mrk 79, as pointed out above, even though it is more distant than NGC 4151, the correlation with the radio jet is clearly seen in the channel maps as well as in the velocity dispersion maps.

4.2 Mass of the ionized and molecular gas

The mass of the ionized and molecular gas can be estimated from the measured fluxes of the Brγ and $H_2\lambda2.1218$ μm emission lines (Riffel et al. 2008; Storchi-Bergmann et al. 2009; Riffel & Storchi-Bergmann 2011b). Following Storchi-Bergmann et al. (2009), we estimate the mass of ionized gas in the inner 1.3 × 1.3 kpc^2 of Mrk 79 by

$$\frac{M_{\rm H\,II}}{\rm M_\odot} \approx 3\times10^{17}\left(\frac{F_{\rm Br\gamma}}{\rm erg\,s^{-1}cm^{-2}}\right)\left(\frac{d}{\rm Mpc}\right)^2, \quad (2)$$

where $F_{\rm Br\gamma}$ is the integrated flux for the Brγ emission line and d is the distance to Mrk 79. We have assumed an electron temperature $T = 10^4$ K and electron density $N_{\rm e} = 100\,{\rm cm^{-3}}$.

The mass of hot molecular gas can be obtained as

$$\frac{M_{\rm H_2}}{\rm M_\odot} \approx 5.0776\times10^{13}\left(\frac{F_{\rm H_2\lambda2.1218}}{\rm erg\,s^{-1}\,cm^{-2}}\right)\left(\frac{d}{\rm Mpc}\right)^2, \quad (3)$$

where $F_{\rm H_2\lambda2.1218}$ is the integrated flux for the H_2 $\lambda2.1218$ μm emission line and a vibrational temperature of $T = 2000$ K was assumed.

Integrating over the whole IFU field we obtain $F_{\rm Br\gamma} \approx 2.7 \times 10^{-15}$ erg s^{-1} cm^{-2} and $F_{\rm H_2\lambda2.1218} \approx 6.7\times10^{-15}$ erg s^{-1} cm^{-2}, resulting in $M_{\rm H\,II} \approx 7\times10^6\,{\rm M_\odot}$ and $M_{\rm H_2} \approx 3\times10^3\,{\rm M_\odot}$. The mass of molecular gas is 10^3 times smaller than that of ionized gas but this H_2 mass represents only that of hot gas emitting in the near-IR (Storchi-Bergmann et al. 2009; Riffel & Storchi-Bergmann 2011b). The values above are in good agreement with the ones found for other active galaxies (e.g. Riffel et al. 2008, 2010; Storchi-Bergmann et al. 2009; Riffel & Storchi-Bergmann 2011b).

According to Mazzalay et al. (2013) the mass of the cold molecular gas can be estimated as

$$\frac{M_{\rm H_2 cold}}{\rm M_\odot} \approx 1174\left(\frac{L_{\rm H_2\lambda2.1218}}{\rm L_\odot}\right), \quad (4)$$

where $L_{\rm H_2\lambda2.1218}$ is the luminosity of the H_2 line and results $M_{\rm H_2 cold} \approx 2\times10^9\,{\rm M_\odot}$ for Mrk 79. The ratio between the cold and hot molecular mass is thus 7×10^5, being within the range of values found for active galaxies in general (Dale et al. 2005; Mazzalay et al. 2013).

4.3 Kinematics of the emitting gas

The velocity field of the molecular gas is completely distinct from that of the ionized gas (Fig. 5). Although both of them present blueshifts of up to −150 km s^{-1} to the south of the nucleus, to the north the molecular gas presents redshifts of up to 150 km s^{-1} in an approximate rotation pattern while the ionized gas presents instead similar blueshifts to those observed to the south. (The [Fe II] does not present much extended emission to the north of the nucleus and thus it was not possible to study its centroid velocity at these locations.) Adopting the systemic velocity derived from the H_2 velocity field,

we find redshifts of up to 50 km s^{-1} around the nucleus for [Fe II] and Paβ.

A distinct kinematics for the H_2, [Fe II] and Paβ emitting gas is also supported by the σ maps (Fig. 6), which show that, at most locations, the H_2 presents the smallest σ values ($\approx$70 km s^{-1}), followed by Paβ ($\approx$100–180 km s^{-1}), with [Fe II] presenting the highest σ values ($\approx$150–180 km s^{-1}), which are correlated with the radio continuum emission. Differences in the velocity fields are also observed in the channel maps (Figs 7, 8 and 9). The [Fe II] emission in all velocity channels is well correlated with the radio image, supporting an interaction between the radio jet and the emitting gas, which is probably being pushed away from the nucleus by the radio jet. The accelerated particles which give origin to the radio emission also contribute to release the iron (Fe) from dust grains, enhancing the [Fe II] emission. In order to destroy the dust grains and release the Fe, fast shocks are necessary. The line ratio [Fe II]/[P II]λ1.18 μm is useful to investigate the role of shocks for the [Fe II] emission. Ratios larger than 2 indicate that shocks have passed through the gas destroying the dust grains, releasing the Fe and thus enhancing its observed abundance (Oliva et al. 2001; Storchi-Bergmann et al. 2009). For Mrk 79 the [Fe II]/[P II] is larger than this value for the extranuclear spectra, as seen in Table 1, indicating the presence of shocks, while for the nucleus the ratio is $\approx$1.6, suggesting that much of the Fe is still locked in dust grains.

The distinct kinematics for the H_2, Paβ and [Fe II] emitting gas support that these gas phases are mostly located in distinct regions of the galaxy. These kinematics properties are similar to those we have found for other active galaxies in previous studies (Storchi-Bergmann et al. 1999, 2009, 2010; Rodríguez-Ardila et al. 2004, 2005; Riffel et al. 2006a, 2008, 2009; Storchi-Bergmann 2010; Riffel & Storchi-Bergmann 2011a,b): the H_2 kinematics is usually dominated by rotation in the galaxy disc while the [Fe II] emitting gas has distinct kinematic components attributed to gas extending to high galactic latitudes, usually in outflow and in interaction with a radio jet. For example, Hicks et al. (2009) have studied the H_2 kinematics from the inner $\approx$100 pc of a sample of nine Seyfert galaxies using the instrument Spectrograph for INtegral Field Observations in the Near Infrared (SINFONI) at the European Southern Observatory Very Large Telescope and also concluded that it is dominated by rotation in a disc with typical radius of $\approx$30 pc and a comparable height.

4.3.1 Feeding

The low σ values, rotation pattern, the location in the plane of the galaxy, as well as the presence of spiral arms in the H_2 emitting gas supports the identification of H_2 as a tracer of the cold gas which feeds the AGN. The H_2 velocity field (right-hand panel of Fig. 5) presents a rotation pattern with the northwest side receding and the southeast side approaching. From this observed velocity field and assuming that the spiral arms of Mrk 79 are trailing it can be concluded that the near side of the galaxy is the northeast and the far side is the southwest as labelled in the top-left panel of Fig. 9. The rotation pattern and low σ support a location of the molecular gas in the plane of the galaxy, and thus the spiral arm seen in blueshift to the southwest (far side) and the other seen in redshift to the northeast can be interpreted as tracing inflows towards the centre of Mrk 79. Similar inflows along spiral arms at scales of tens to hundreds of parsecs have also been observed in other galaxies in ionized gas at optical wavelengths (Fathi et al. 2006; Storchi-Bergmann et al. 2007; van de Ven & Fathi 2010; Müller et al. 2011) and in molecular gas in the near-IR (Riffel et al. 2008; Davies et al. 2009; Sánchez et al. 2009; Riffel & Storchi-Bergmann 2011a). Following Riffel et al. (2008), we estimate the hot molecular gas mass inflow rate through a circular cross-section as

$$\dot{M}_{H_2} = 2 m_p N_{H_2} v \pi r^2 n_{arms}, \quad (5)$$

where $v = v_{obs}/\sin i$ is the velocity of the inflowing material in the plane of the galaxy, v_{obs} is the observed velocity, i is the inclination of the disc, r is the radius of the circular cross-section, N_{H_2} is the hot H_2 density, m_p is the proton mass and $n_{arms} = 2$ is the number of spiral arms.

N_{H_2} can be estimated from the mass of hot molecular gas under the assumption that it is located in a disc with radius $r_d \approx 1$ arcsec = 455 pc (as observed in the H_2 flux map in Fig. 3) and height h = 30 pc, as suggested by Hicks et al. (2009) for H_2 discs observed in the inner few tens of parsec of active galaxies by near-IR integral field spectroscopy. The resulting average hot H_2 density is $N_{H_2} = \frac{M_{H_2}}{2 m_p \pi r_d^2 h} = 3.13 \times 10^{-3}$ cm^{-3}.

The radius of the cross-section can be obtained from Fig. 9 as the half of the width of the spiral arms $r \approx 0.3$ arcsec $\approx$ 135 pc. Adopting $v_{obs} \approx 120$ km s^{-1}(Fig. 9), we obtain $\dot{M}_{H_2} \approx 2 \times 10^{-3}\,M_\odot\,yr^{-1}/\sin i$. Assuming that the inclination of the H_2 disc is $i \approx 30^\circ$ (Paturel et al. 2003) the mass inflow rate is $\dot{M}_{H_2} \approx 4 \times 10^{-3}\,M_\odot\,yr^{-1}$. This value is within the range of molecular gas mass inflow rates found for other active galaxies (Fathi et al. 2006; Storchi-Bergmann et al. 2007; Riffel et al. 2008; Davies et al. 2009; Sánchez et al. 2009; van de Ven & Fathi 2010).

4.3.2 Feedback

As discussed above, the velocity fields for the ionized gas of Fig. 5 are not compatible with pure rotation in the galactic disc as in the case of H_2. For Paβ blueshifts are observed to both sides of the nucleus, although with less extended emission to the north. In the channel maps, to the south of the nucleus, the blueshifts observed for the ionized gas (both for Paβ and [Fe II]) are similar to those of the H_2 velocity field and thus we conclude that this emission is dominated by gas in rotation in the plane of the galaxy. On the other hand, there is also gas in redshift to the south, which cannot be in the plane and we interpret as due to an outflow projected against the far side of the galaxy. The emission in blueshift to the north, observed in the Paβ channel maps may be interpreted as due to the counterpart of the southern outflow observed in redshift; the outflow to the north is thus oriented towards us. The redshifts to the north of the nucleus seen in the Paβ velocity field have approximately the same velocities as those observed for the H_2 at the same location and is probably due to emission from the disc.

We can estimate the mass outflow rate across a circular cross-section with radius $r = 0.7$ arcsec $\approx$ 320 pc located at a distance of 1.0 arcsec from the nucleus to the north, corresponding to an opening angle of 35°, obtained directly from the middle panel of Fig. 5, by

$$\dot{M}_{out} = \frac{m_p N_e v_{obs} f A}{\sin\theta}, \quad (6)$$

where m_p is the proton mass, N_e the electron density, v_{obs} is the observed velocity for the outflow, f is the filling factor, A is the area of the cross-section and θ is the inclination of the cone axis relative to the plane of the sky (Riffel & Storchi-Bergmann 2011a). Assuming $N_e = 500$ cm^{-3}, $f = 0.01$ and $v_{out} = 75$ km s^{-1}, directly from middle panel of Fig. 5, we obtain $\dot{M}_{out} \approx 3/\sin\theta\ M_\odot\ yr^{-1}$.

Bian & Zhao (2002) pointed out that the inclination of the accretion disc of Mrk 79 is ≈30.°6 assuming that the broad-line region has a Keplerian velocity and using the FWHM from the broad component of Hβ, suggesting that the accretion disc has approximately the same orientation of the large-scale disc (Paturel et al. 2003). Assuming that the cone axis is perpendicular to de accretion disc, we obtain $\theta \approx 60^\circ$ and thus, the mass outflow rate would be $\dot{M}_{\rm out} \approx 3.5\,{\rm M}_\odot\,{\rm yr}^{-1}$. This value is in the range of mass outflow rates observed for other active galaxies (Veilleux, Cecil & Bland-Hawthorn 2005; Crenshaw & Kraemer 2007; Barbosa et al. 2009; Riffel et al. 2009; Storchi-Bergmann et al. 2010; Riffel & Storchi-Bergmann 2011a).

Following Storchi-Bergmann et al. (2010), we can use the above mass outflow rate to estimate the kinetic power of the outflow by

$$\dot{E} \approx \frac{\dot{M}_{\rm out}}{2}(v_{\rm out}^2 + \sigma^2), \quad (7)$$

where $v_{\rm out} = v_{\rm obs}/\sin\theta$ is the velocity of the outflowing gas and σ is its velocity dispersion. Using $\sigma \approx 150\,{\rm km\,s^{-1}}$ (from Fig. 6) and $v_{\rm out} = v_{\rm obs}/\sin\theta = 75\,{\rm km\,s^{-1}}/\sin 60^\circ = 75\,{\rm km\,s^{-1}}$ we obtain $\dot{E} \approx 3.4 \times 10^{40}$ erg s^{-1}, which is in good agreement with those obtained for Seyfert galaxies and compact radio sources (Morganti, Tadhunter & Oosterloo 2005; Holt et al. 2006; Storchi-Bergmann et al. 2010; Holt et al. 2011; Riffel & Storchi-Bergmann 2011b).

4.3.3 Mass accretion rate

The accretion rate necessary to power the AGN at the nucleus of Mrk 79 can be obtained from

$$\dot{m} = \frac{L_{\rm bol}}{c^2\eta}, \quad (8)$$

where $L_{\rm bol}$ is the nuclear bolometric luminosity, η is the efficiency of conversion of the rest mass energy of the accreted material into radiation and c is the light speed. The bolometric luminosity for Mrk 79 is $L_{\rm bol} \approx 2 \times 10^{44}\,{\rm erg\,s^{-1}}$ (Zhou & Zhao 2010). Assuming $\eta \approx 0.1$ (e.g. Frank, King & Raine 2002), we obtain a mass accretion rate of $\dot{m} \approx 3.5 \times 10^{-2}\,{\rm M}_\odot\,{\rm yr}^{-1}$.

We can compare the mass accretion rate with the mass inflow and outflow rates estimated in Sections 4.3.1 and 4.3.2, respectively. The mass inflow rate for the hot molecular gas is one order of magnitude smaller than the accretion rate. As discussed in our previous studies, the total mass inflow rate may be larger than the one observed in hot molecular gas, since large amounts of cold molecular gas are observed in central region of active galaxies (e.g. Dale et al. 2005; Boone et al. 2007; Krips et al. 2007; Mazzalay et al. 2013). On the other hand, the mass outflow rate in the NLR of Mrk 79 is about two orders of magnitude larger than $\dot{m}$, a ratio comparable to those observed for other Seyfert galaxies, which indicates that most of the outflowing gas observed in the NLR of active galaxies does not originate in the AGN but in the ISM surrounding the galaxy nucleus, which is pushed away by the AGN outflow (e.g. Riffel & Storchi-Bergmann 2011b).

Finally, comparing the kinetic power with the bolometric luminosity we find that $\dot{E}$ is four orders of magnitude smaller than $L_{\rm bol}$, implying that only a small fraction of the mass accretion rate is transformed in kinetic power in the NLR outflows. This value is in reasonable agreement with the AGN feedback derived by Di Matteo, Springel & Hernquist (2005) in simulations for the coevolution of black holes and galaxies, in order to match the $M-\sigma$ relation and similar to those derived for Seyfert galaxies using optical integral field spectroscopy (Barbosa et al. 2009), after revising the filling factor and gas density values as in Riffel & Storchi-Bergmann (2011b).

5 CONCLUSIONS

We have analysed two-dimensional near-IR J and $K_{\rm l}$ bands spectra from the inner ≈680 pc radius of the Seyfert 1 galaxy Mrk 79 obtained with the Gemini NIFS at a spatial resolution of ≈100 pc (0.25 arcsec) and velocity resolution of ≈35−45 km s^{-1}. We have mapped the emission-line flux distributions and ratios, as well as the kinematics of the molecular and ionized emitting gas. The main conclusions of this work are as follows.

(i) The coronal line emission is marginally resolved by our observations, being more extended to the north–south direction – following the same orientation of the radio jet, reaching ≈450 pc from the nucleus.

(ii) The [Fe II] and [P II] emission are well correlated with the radio emission, while the H I recombination lines are better correlated with the [O III] emission.

(iii) We detected two nuclear spiral arms in the H_2 flux distribution, extending by 680 pc, one to the south of the nucleus and another to the north. These arms begin in a nuclear bar with extent of ≈400 pc oriented along the east–west direction.

(iv) The excitation of the H_2 and [Fe II] lines is due to heating of the gas by X-rays from the central AGN. A small contribution from shocks due to the interaction of the radio jet with the ISM may also contribute to the [Fe II] emission, as evidenced by enhancements in the [Fe II] flux and σ at locations cospatial with radio structures.

(v) The kinematics of the H_2 is dominated by rotation, with inflows along the nuclear spiral arms with a mass inflow rate of $\dot{M}_{\rm H_2} \approx 4 \times 10^{-3}\,{\rm M}_\odot\,{\rm yr}^{-1}$, comparable to the mass accretion rate necessary to power the AGN of Mrk 79 ($\dot{m} \approx 1.3 \times 10^{-3}\,{\rm M}_\odot\,{\rm yr}^{-1}$).

(vi) The kinematics of the ionized gas not only shows a rotation component to the south, which is probably in the galaxy plane, but also shows an outflow component, observed in redshift to the south and in blueshift to the north of the nucleus. The ionized gas mass outflow rate through a cross-section with radius ≈320 pc located at a distance of ≈455 pc from the nucleus is $\dot{M}_{\rm out} \approx 3.5\,{\rm M}_\odot\,{\rm yr}^{-1}$, indicating that most of this outflowing gas originates in the ISM surrounding the galaxy nucleus, which is pushed by the AGN outflow.

(vii) The kinetic power of the outflow is four orders of magnitude smaller than the bolometric luminosity of the AGN of Mrk 79, implying that only a small fraction of the mass accretion rate is transformed in kinetic power in the NLR outflows.

ACKNOWLEDGEMENTS

We thank an anonymous referee for useful suggestions which helped to improve the paper. This work is based on observations obtained at the Gemini Observatory, which is operated by the Association of Universities for Research in Astronomy, Inc., under a cooperative agreement with the NSF on behalf of the Gemini partnership: the National Science Foundation (USA), the Science and Technology Facilities Council (UK), the National Research Council (Canada), CONICYT (Chile), the Australian Research Council (Australia), Ministério da Ciência e Tecnologia (Brazil) and southeast CYT (Argentina). This research has made use of the NASA/IPAC Extragalactic Database (NED) which is operated by the Jet Propulsion Laboratory, California Institute of Technology, under contract with

the National Aeronautics and Space Administration. This work has been partially supported by the Brazilian institution CNPq.

REFERENCES

Barbosa F. K. B., Storchi-Bergmann T., Cid Fernandes R., Winge C., Schmitt H., 2009, MNRAS, 396, 2
Bian W., Zhao Y., 2002, A&A, 395, 465
Black J. H., van Dishoeck E. F., 1987, ApJ, 322, 412
Boone F. et al., 2007, A&A, 471, 113
Cardelli J. A., Clayton G. C., Mathis J. S., 1989, ApJ, 345, 245
Crenshaw D. M., Kraemer S. B., 2007, ApJ, 659, 250
Dale D. A., Sheth K., Helou G., Regan M. W., Hüttemeister S., 2005, ApJ, 129, 2197
Das V. et al., 2005, AJ, 130, 945
Das V., Crenshaw D. M., Kraemer S. B., Deo R. P., 2006, AJ, 132, 620
Davies R. I., Maciejewski W., Hicks E. K. S., Tacconi L. J., Genzel R., Engel H., 2009, ApJ, 702, 114
de Vaucouleurs G., de Vaucouleurs A., Corwin H. G., Jr, Buta R. J., Paturel G., Fouque P., 1991, Third Reference Catalogue of Bright Galaxies. Springer-Verlag, Berlin
Di Matteo T., Springel V., Hernquist L., 2005, Nat, 433, 604
Dors O. L., Riffel R. A., Cardaci M. C., Hägele G. F., Krabbe A. C., Pérez-Montero E., Rodrigues I., 2012, MNRAS, 422, 252
Fathi K., Storchi-Bergmann T., Riffel R. A., Winge C., Axon D. J., Robinson A., Capetti A., Marconi A., 2006, ApJ, 641, L25
Forbes D. A., Ward M. J., 1993, ApJ, 416, 150
Frank J., King A. R., Raine D. J., 2002, Accretion Power in Astrophysics, 3rd edn. Cambridge Univ. Press, Cambridge
Fritz J., Franceschini A., Hatziminaoglou E., 2006, MNRAS, 366, 767
Haniff C. A., Wilson A. S., Ward M. J., 1988, ApJ, 334, 104
Hicks E. K. S., Davies R. I., Malkan M. A., Genzel R., Tacconi L. J., Sánchez F. M., Sternberg A., 2009, ApJ, 696, 448
Hollenbach D., McKee C. F., 1989, ApJ, 342, 306
Holt J., Tadhunter C., Morganti R., Bellamy M., González Delgado R. M., Tzioumis A., Inskip K. J., 2006, MNRAS, 370, 1633
Holt J., Tadhunter C. N., Morganti R., Emonts B. H., 2011, MNRAS, 410, 1527
Hunt L. K., Malkan M. A., Rush B., Bicay M. D., Nelson B. O., Stanga R. M., Webb W., 1999, ApJS, 125, 349
Kaiser M. E. et al., 2000, ApJ, 528, 260
Kraemer S. B., Schmitt H. R., Crenshaw M. D., Meléndez M., Turner T. J., Guainazzi M., Mushotzky R. F, 2011, ApJ, 727, 130
Krips M. et al., 2007, A&A, 468, 63
Larkin J. E., Armus L., Knop R. A., Soifer B. T., Matthews K., 1998, ApJS, 114, 59
Maloney P. R., Hollenbach D. J., Tielens A. G. G. M., 1996, ApJ, 466, 561
Mazzalay X. et al., 2013, MNRAS, 428, 2389
McGregor P. J. et al., 2003, Proc. SPIE, 4841, 1581
MÏller A. S., Storchi-Bergmann T., Riffel R. A., Ferrari F., Axon D., Robinson A., 2011, MNRAS, 413, 149
Morganti R., Tadhunter C. N., Oosterloo T. A., 2005, A&A, 444, L9
Mouri H., 1994, ApJ, 427, 777
Nagar N. M., Wilson A. S., Mulchaey J. S., Gallimore J. F., 1999, ApJS, 120, 209
Oliva E. et al., 2001, A&A, 369, L5
Osterbrock D. E., Ferland G. J., 2006, Astrophysics of Gaseous Nebulae and Active Galactic Nuclei, 2nd edn. University Science Books, Mill Valley, CA
Paturel G., Petit C., Prugniel Ph., Theureau G., Rousseau J., Brouty M., Dubois P., Cambrésy L., 2003, A&A, 412, 45
Peterson B. M. et al., 2004, ApJ, 613, 682
Ramos Almeida C., Pérez García A. M., Acosta-Pulido J. A., 2009, ApJ, 694, 1379
Riffel R. A., 2010, Ap&SS, 327, 239
Riffel R. A., Storchi-Bergmann T., 2011a, MNRAS, 411, 469
Riffel R. A., Storchi-Bergmann T., 2011b, MNRAS, 417, 2752
Riffel R. A., Storchi-Bergmann T., 2011c, in Romero G. E., Sunyaev R. A., Belloni T. M., eds, Proc. IAU Meeting 275, Jets at all Scales. Cambridge Univ. Press, Cambridge, p. 172
Riffel R. A., Sorchi-Bergmann T., Winge C., Barbosa F. K. B., 2006a, MNRAS, 373, 2
Riffel R., Rodríguez-Ardila A., Pastoriza M. G., 2006b, A&A, 457, 61
Riffel R. A., Storchi-Bergmann T., Winge C., McGregor P. J., Beck T., Schmitt H., 2008, MNRAS, 385, 1129
Riffel R. A., Storchi-Bergmann T., Dors O. L., Winge C., 2009, MNRAS, 393, 783
Riffel R. A., Storchi-Bergmann T., Nagar N. M., 2010, MNRAS, 404, 166
Rodríguez-Ardila A., Pastoriza M. G., Viegas S., Sigut T. A. A., Pradhan A. K., 2004, A&A, 425, 457
Rodríguez-Ardila A., Riffel R., Pastoriza M. G., 2005, MNRAS, 364, 1041
Rodríguez-Ardila A., Prieto M. A., Viegas S., Gruenwald R., 2006, ApJ, 653, 1098
Sánchez F. M., Davies R. I., Genzel R., Tacconi L. J., Eisenhauer F., Hicks E. K. S., Friedrich S., Sternberg A., 2009, ApJ, 691, 749
Schmitt H. R., Ulvestad J. S., Antonucci R. R. J., Kinney A. L., 2001, ApJS, 132, 199
Schmitt H. R., Donley J. L., Antonucci R. R. J., Hutchings J. B., Kinney A. L., 2003, ApJS, 148, 327
Simpson C., Forbes D. A., Baker A. C., Ward M. J., 1996, MNRAS, 283, 777
Storchi-Bergmann T., 2010, Proc. IAU Meeting 267, Co-Evolution of Central Black Holes and Galaxies. Cambridge Univ. Press, Cambridge, p. 290
Storchi-Bergmann T., Winge C., Ward M., Wilson A. S., 1999, MNRAS, 304, 35
Storchi-Bergmann T., Dors O., Jr, Riffel R. A., Fathi K., Axon D. J., Robinson A., 2007, ApJ, 670, 959
Storchi-Bergmann T., McGregor P., Riffel R. A., Simões Lopes R., Beck T., Dopita M., 2009, MNRAS, 394, 1148
Storchi-Bergmann T., Simões Lopes R., McGregor P., Riffel R. A., Beck T., Martini P., 2010, MNRAS, 402, 819
Ulvestad J. S., Wilson A. S., 1984, ApJ, 285, 439
van de Ven G., Fathi K., 2010, ApJ, 723, 767
Veilleux S., Cecil G., Bland-Hawthorn J., 2005, ARA&A, 43, 769
Whittle M., Pedlar A., Meurs E. J. A., Unger S. W., Axon D. J., Ward M. J., 1988, ApJ, 326, 125
Zhou X., Zhao Y., 2010, ApJ, 720, 206

This paper has been typeset from a TEX/LATEX file prepared by the author.